Structure and properties of two superionic ice phases

Vitali B. Prakapenka[1*], Nicholas Holtgrewe[1,2], Sergey S. Lobanov[2,3], Alexander Goncharov[2*]

[1]Center for Advanced Radiations Sources, University of Chicago, Chicago, Illinois 60637, USA.
[2]Earth and Planets Laboratory, Carnegie Institution of Washington, Washington, DC 20015, USA.
[3]GFZ German Research Center for Geosciences, Telegrafenberg, 14473 Potsdam, Germany.
[*]**Corresponding authors: Email: agoncharov@carnegiescience.edu**
prakapenka@cars.uchicago.edu

Abstract.

In the phase diagram of water, superionic ices with highly mobile protons within the stable oxygen sublattice have been predicted at high pressures. However, the existence of superionic ices and the location of the melting line have been challenging to determine from both theory and experiments, yielding contradictory results depending on the employed techniques and the interpretation of the data. Here, we report high pressure and high temperature synchrotron X-ray diffraction and optical spectroscopy measurements of water in a laser-heated diamond anvil cell, and reveal first-order phase transitions to ices with body-centred and face-centred cubic oxygen lattices. Based on the distinct density, increased optical conductivity and the greatly decreased fusion enthalpies, we assign these observed structures to the theoretically predicted superionic ice phases. Our measurements determine the pressure–temperature stability fields of superionic ice phases and the melting line, suggesting the presence of face-centred cubic superionic ice in water-rich giant planets, such as Neptune and Uranus. The melting line determined here is at higher temperatures than previously determined in static compression experiments, but it is in agreement with theoretical calculations and data from shock wave experiments.

Main Text:

Ice at extreme pressure-temperature (P-T) conditions experiences a dramatic modification from a hydrogen bonded molecular dipole form to nonmolecular "extended" structures [1-6]. Upon the breakdown of strong covalent intramolecular bonding and the formation of ionic solids, *e.g.* symmetric ice X [1,4,7], the quantum and thermal proton motions become comparable in energy. This change in the energy landscape results in stability of superionic phases [3], which are characterized by a large proton mobility within solid oxygen sublattice and, thus, ionic conductivity. The theoretically predicted superionic states of H_2O are expected to appear at high pressures and high temperatures and interface the stability fields of solid ices and fluid water. The existence of superionic ices in nature has important consequences for the interior of ice giant planets, where generation of magnetic field is thought to be related to the presence of shallow fluid convective layers [3,8,9].

Several aspects of the phase diagram of water at high pressure are immensely controversial: the location of the melting line [5,10-18] and the existence, structure, physical nature, and location of

solid phase(s) in equilibrium with the fluid phase. Experimental and theoretical determinations of the melting line vary by up to 700 K (at approximately 50 GPa) and there are no reported measurements above 90 GPa, except a single point near 5000 K at 190 GPa derived from shock-wave experiments in pre-compressed water [19] (Supplementary Figs. 1-2). The experiments agree that there is a sudden increase in the slope of the melting line at 20-47 GPa [5,10,12,13,17,18]; however, the origin of this anomaly and its location remain controversial. It has been assigned to a triple point between the fluid, ice VII, and ice X [10,12] (or dynamically disordered ice VII′ [4,6,20]), while other works suggest that it is related to a triple point between the fluid, ice VII, and superionic ice [5,21-23]. Moreover, there are reports about the existence of another triple point near 20 GPa and 800 K and an additional solid phase with unknown properties [12]. Rigid water models and *ab initio* calculations predict the existence of plastic ice phases with body-centred and face-centred cubic (*bcc* and *fcc*, respectively) oxygen lattices and freely rotating molecules at pressures above 2 GPa and 300 K [24-26]. Hereafter, "*bcc"* and "*fcc"* refer to both plastic and superionic phases. On the other hand, above 20 GPa and 1000 K, other *ab initio* simulations suggest that ice VII and the fluid are interfaced in the phase diagram by superionic phase(s) characterized by a large proton diffusivity [3,8,21,25-30] (Supplementary Fig. 2). The theoretically predicted superionic phases are also expected to show polymorphism above 100 GPa [30-32]. Recent dynamic compression X-ray diffraction (XRD) experiments between 160 and 420 GPa report a transformation from a *bcc* ice X to a *fcc* superionic ice [33]. Finally, recent static experiments reported an isostructural transition of ice VII at high temperatures to a *bcc* structure with larger volume and entropy, suggesting that it is superionic [34]. Overall, existing experimental data and theoretical calculations show an extreme diversity concerning proton dynamics and conductivity and polymorphism of water and ices (Supplementary Figs. 1-2) and thus call for further experimental investigations.

Here we report the results of combined synchrotron XRD and optical spectroscopy studies in the laser heated diamond anvil cell (DAC) up to 150 GPa and 6500 K. The measurements probe *in situ* structural and electronic properties of H_2O ices and fluid at these conditions, shedding light on the phase diagram and the transport properties of water at extremes. Our experiments reveal and map out the stability fields of two solid phases at elevated temperatures above 20 GPa, which are distinct in density from the familiar ices and the fluid. We assign these phases to the theoretically predicted superionic ices based on their excessive entropy and the P-T conditions of stability. The superionic nature of these phases is supported by our optical spectroscopy measurements, revealing that these phases are moderately absorptive. The same experiments detect a strong absorption threshold, which corresponds to the onset of electronic conductivity in fluid at about 4500 K.

Our extensive XRD experiments in H_2O (Methods) at various P-T conditions (Supplementary Table 1) probe the ice structures and melting up to 150 GPa (Fig. 1). Below 20 GPa, ice VII is the only crystalline phase above room temperature, and it melts at the lowest reachable/detectable temperatures, in good agreement with available literature data (Supplementary Fig. 1). Laser heating experiments (Methods) at pressures above 20 GPa reveal two phase boundaries. In the pressure range of ~20-60 GPa and upon heating to 900-1900 K, we detect a first-order transformation of ice VII to another *bcc* phase with lower density via an abrupt discontinuous shift of the Bragg reflections (Fig. 2(a), Supplementary Fig. 3 and

Supplementary Table 2); up to three peaks of *bcc* phase of lower density are observed (Supplementary Fig. 6). This occurs at the P-T conditions where the majority of previous static compression measurements detected an anomaly, which was assigned to melting [5,14,15,17,18] (Supplementary Fig. 1). Temperature increases slowly with pressure along this phase transition line to 42 GPa, at which point the phase line shows an abrupt increase in slope (Fig. 1). The low-density *bcc* phase of ice discovered in our study, which we name *bcc*-SI (superionic), or ice XX (c.f. Ref. [33]) hereafter, melts along the line rising with pressure very close to that measured in Refs. [10,13] up to approximately 30 GPa (Supplementary Fig. 1).

At P≥29 GPa and T≥1300 K, we have observed another solid phase, which was synthesized in a region of phase space adjacent to the stability field of *bcc*-SI, and at higher temperatures (Figs. 1, 2(b), Supplementary Figs. 4-6). Up to five reflections (in selected experiments) were used to identify the *fcc* structure of this phase (Fig. 2, Supplementary Figs. 4-6), which we call *fcc*-SI or ice XVIII hereafter (c.f. Ref. [33], where only one Bragg reflection assigned to *fcc* phase was detected). At pressures above 29 GPa and below 60 GPa, the sequence of temperature-induced phase transitions of H_2O is the following: ice-VII(VII′) – *bcc*-SI – *fcc*-SI – fluid (Figs. 1, 2(a)). At higher pressures, the temperature stability range of *fcc*-SI increases, while that of the *bcc*-SI phase decreases and eventually vanishes above 60 GPa, where *fcc*-SI is the only stable superionic phase.

Our laser heating experiments combined with XRD measurements detect melting via an abrupt and almost complete disappearance of the Bragg peaks (Supplementary Fig. 3(b)) and emergence of the first diffuse peak (Fig. 2(b), Supplementary Figs. 3(c), 5, 7). However, above approximately 60 GPa only a partial melting could be observed because of large axial temperature gradients (Methods, Supplementary Fig. 5)) and lack of thermal insulation. Our measurements indicate an abrupt increase in slope of the melting line above 29 GPa (Fig. 1), where the *fcc*-SI phase appears at higher temperature than *bcc*-SI and thus becomes the phase which melts (cf. Ref. [10]). Also, we find that the transition line between the high density *bcc* ice (VII′ or X) and *fcc*-SI and *bcc*-SI phases rises steeply above 42 GPa due to an increase in slope of the phase line related to the transition between molecular ice VII and dynamically disordered symmetric ice VII′ [5,6]. The latter is similar to ice X but is expected to have a bimodal proton distribution [4]. This is qualitatively consistent with the previous observations, though they were interpreted as a change in slope of the melting line [5,17,18] (Supplementary Fig. 1), and disagrees with theoretical calculations, which predict a very flat or even negative slope of this phase line [3,30,31] (Supplementary Fig. 2). Overall, our P-T phase diagram includes two superionic ices, *bcc*-SI and *fcc*-SI (cf. Ref. [34]), and four triple points: VII—*bcc*-SI— fluid, *bcc*-SI—*fcc*-SI— fluid, *bcc*-SI—*fcc*-SI—VII′ (X), and VII—VII′ (X)—*bcc*-SI. These features of the phase diagram resolve previous inconsistency in data interpretations (see Supplementary Table 3 for the phase lines deduced here). These transformations are fully reversible; they are identified by XRD measurements upon heating, upon cooling, and upon quenching to 300 K (Fig. 2 and Supplementary Figs. 3(b), 5).

The unit cell volumes (densities) of the observed here *bcc*-SI and *fcc*-SI phases are quite distinct from those of ice VII (VII′ or X at higher pressure) (Methods, Fig. 3; Supplementary Figs. 8-9

and Supplementary Table 4). The densities of SI phases are between those of low-temperature ices and the fluid, the latter being inferred from previous experiments [19,22] (Supplementary Table 4) and the positions of the first sharp diffraction peak of fluid water (Supplementary Figs. 7, 8). The thermal expansion effects in ices VII and X (*e.g.* measured up to 100 GPa and 900 K in Refs. [14,23]) are smaller compared to the large and discontinuous volume expansions of *bcc* lattices upon transformation to *bcc*-SI and *fcc*-SI phases (Supplementary Figs. 8-9) and thus can be sorted out. The density (specific volume) of SI phases was measured in a broad temperature range in our experiments (900-4600 K) depending on pressure (Fig. 1), which can affect the results. However, only moderate thermal expansion of ices VII and X (reduced by the thermal pressure) were observed along our experimental P-T pathways (Fig. 2 and Supplementary Fig. 9), suggesting moderate thermal expansion effects in the SI ices probed here. In addition, the stability domains of SI ices is relatively narrow in temperature (Fig. 1). Our experiments show that the densities of *bcc*-SI and *fcc*-SI are very close to each other in the pressure range where both phases can exist (Fig. 1) and these data can be represented by the same curve (Fig. 3), indicating that these two phases have similar nature and evidencing that *bcc*-SI is not a thermally expanded ice VII(X). The densities of SI ice inferred from the shock velocimetry along the Hugoniot [19] are slightly smaller compared to our data extrapolated to 185 GPa, but they agree within the error bars (Fig. 3), which include uncertainty in the thermal pressure in our experiments. On the other hand, the densities of *fcc*-SI ice inferred from the position of one XRD peak in the reverberation compression experiments [33] agree well with our extrapolated data. However, these data are reported at substantially lower temperatures than in our experiments (Supplementary Fig. 10). Theoretically computed Equations of States (EOS) of *bcc*-SI [25,27] at 1300-2000 K agree well with our results (Supplementary Fig. 8). However, the computed volume discontinuity due to the transformation to SI phase is smaller than the discontinuity observed in the present experiments (Fig. 3, Supplementary Figs. 8, 9).

The phase diagram and EOSs of various phases obtained here (Supplementary Tables 3-4) can be used to understand the nature of two high-temperature ice phases, which are predicted to be superionic and appear upon heating of common dense ices above 20 GPa. Although our XRD data do not directly probe the positions of hydrogen atoms, we can infer the mobility of hydrogen in SI phases by assessing the entropy change of the melting (*e.g.* Refs. [22,36]). We obtain the enthalpy of fusion (latent heat), ΔH_f, from the Clausius–Clapeyron relation

$$\frac{dP_m}{dT} = \frac{\Delta H_f}{T\Delta V}$$

where P_m is the pressure along the melting line and ΔV is the volume change due to melting. Below 18 GPa, where molecular and dielectric ice VII melts directly to an ionized water [21,33] (Fig. 1), ΔH_f increases very fast with pressure (Supplementary Fig. 11). At higher pressures, where *bcc*-SI appears and separates ice VII and fluid in the phase diagram, the melting line starts rising steeper, leading to a substantial drop of the enthalpy of fusion, which then increases with pressure gradually; a similar behavior occurs upon the appearance of *fcc*-SI phase. Fluid water is not expected to have an abrupt change in entropy over the pressure range of transitions to *bcc*-SI and *fcc*-SI, and there is no anomaly in the ΔV (Fig. 3). Thus, we conclude that abrupt changes in ΔH_f are due to an increase of entropy in *bcc*-SI and *fcc*-SI, especially in *bcc*-SI compared to ice

VII: 62 kJ/mole vs 19 kJ/mole for transitions to *bcc*-SI and *fcc*-SI, respectively. This points to the superionic nature of *bcc*-SI and *fcc*-SI phases as predicted theoretically [3,8,21,25,28-32,35] and inferred based on experimental data [5,19,22,23,33,34]. The phase diagram of water is qualitatively similar to that of ammonia [3] in that both demonstrate the presence of superionic phases at extreme P-T conditions. However, our experiments show that SI phase of water emerges at lower pressure and slightly higher temperature than in ammonia [36] (Supplementary Fig. 12). It appears that the stability range of a plastic phase of water (if any) is greatly reduced compared to ammonia, likely because of the presence of the strong hydrogen bonds.

To assess the electronic properties of ices and fluid water, we directly probed the optical conductivity using visible/near IR absorption with a white pulsed laser (supercontinuum) spectroscopy in the pulsed laser heated DAC (Methods). An optical conductivity as low as 5 S/cm, which is near the lower limit expected for a superionic phase [19], could be detected in these experiments (Methods). Our time domain absorption spectra measured on cooling down in close to equilibrium P-T conditions (Fig. 4, Methods, Supplementary Fig. 13), show that there is a sharp temperature boundary at 4000 K. Above 4000 K, water is strongly absorptive, with the optical conductivity >15 S/cm. Similar phenomena are documented in H_2 [37] and N_2 [38], albeit at different temperatures. Upon cooling, the sample becomes less opaque and eventually transparent, indicating a reversible transformation back to an insulating state. However, upon cooling samples heated above 4000 K at 33 and 51 GPa, transmission increases non-monotonously. In fact, a second transmission minimum is detected, which we assign to optical absorption of the SI phases (Supplementary Fig. 13). Fluid water remains non-absorptive below 4000 K, as evidenced from the heating event at 17 GPa, in which transmission increases monotonically to the initial level upon cooling. The temperatures at which these absorptive states of SI ices appear are in a fairly good agreement with the phase lines determined by XRD (Fig. 1). At 17 GPa, which is close to the pressure where the *bcc*-SI phase appears, we observed an intermittent behavior upon cooling; the sample transmission behaves regularly in some single shot events (Supplementary Fig. 13) and shows an anomaly in another. At 105 GPa, the temperature at which the strong absorption edge is detected is very close to the melt line of *fcc*-SI, so these absorptive states of fluid and *fcc*-SI phase are difficult to distinguish. A careful examination suggests that there is a second deep transmission minimum, which we tentatively assign to *fcc*-SI phase absorption based on the time-domain radiative temperature measurements (Supplementary Fig. 13). At 105 GPa the absorptive state of *fcc*-SI phase reverts sharply into transparent ice X near the phase line determined in XRD experiment (Fig. 1, Supplementary Fig. 13).

The optical absorption coefficient of SI ice at 33 and 51 GPa shows an unusual increase toward the lower energy (cf. the spectra of semiconducting H_2 and N_2 [37,38]), which can be tentatively attributed to superionic behavior (Fig. 4a). The physical mechanism of this behavior is unclear; we suggest that is likely due to highly damped low-frequency vibrational modes (*e.g.* O-H stretch), which dramatically broaden and blue shift [5] upon the transition to SI phase(s) (*e.g.* Ref. [39]). However, at 105 GPa, we find much stronger overall absorption and almost energy independent spectra of *fcc*-SI phase, which is characteristic of semiconductors with thermally activated charges (*e.g.* Ref. [40]). The optical conductivity of superionic and fluid phases

determined here corresponds well with optical experiments of Ref. [19] obtained along the ice VII Hugoniot (Fig. 4b). However, we stress that the optical conductivity has a substantial ionic contribution at low temperatures (≤2500 K), where the density of thermally excited charges is small since the electronic band gap is about 4.4 eV [40] (c.f. density functional theory band gap of 2.6 eV [41]). In the limit of high T, our values of conductivity are in a fair agreement with theoretical calculations [3,29,42] and previously reported shock wave electrical conductivity [43-45] and optical [19,46] experiments. One should note, however, that unlike the data presented here, the temperatures in these shock experiments are highly uncertain (except Ref. [19], where it was measured radiometrically).

Our measurements clearly establish a temperature boundary (Fig. 1) beyond which water becomes highly absorptive (likely semiconducting) similar to other materials showing a plasma transition to a conducting fluid state at similar P-T conditions [37,38,47]. These results qualitatively agree with previously reported shock wave experiments [45,46]. However, our experiments, which measure temperature directly, suggest somewhat lower temperatures. Moreover, unlike shock wave experiments, our optical spectroscopy measurements in the laser heated DAC are capable of probing a wide range of P-T conditions and of determining the ionization and superionic phase boundaries directly. Our data reveal the absorptive nature of SI and fluid phases consistent with the ionic and electronic conductivity mechanisms predicted theoretically, while the measured conductivity values are in general agreement with shock results along the Hugoniot [19] (Fig. 4(b), Supplementary Fig. 10). In this regard, we note that the impedance measurements of Ref. [23] suggested much lower temperatures for superionic states within the stability range of ice VII (VII′, X) (Supplementary Fig. 1), while our experiments show an abrupt change into a superionic state along the phase line.

Contrasting to previous static and dynamic experiments, our work provides a clear characterization of the phase and electronic states of water probed at *in situ* P-T conditions with synchrotron XRD combined with direct optical diagnostics. An experimental discovery of *bcc*-SI or ice-XX phase reconciles previous experimental and theoretical contradictions in the position and shape of the melting line. The high-pressure *fcc*-SI (or ice-XVIII) phase has been indisputably identified here by observations of up to five Bragg reflections (Fig. S5) (cf. one reflection of Ref. [33]). The existence of two superionic phases proposed here is in a good agreement with the theoretical predictions [27,31,32] (Supplementary Fig. 2). Albeit, our experiments identify different P-T stability domains, likely because resolving the phase boundary between *bcc*-SI and *fcc*-SI remains a challenge for the theory [30,31]. Our *in situ* synchrotron XRD experiments (Figs. 2, Supplementary Figs. 3-6) clearly show that *fcc*-SI forms at higher T than *bcc*-SI and dominates at high P, while theories suggest that the stability of *fcc*-SI is almost solely P driven (except Ref. [30]). Furthermore, we show that *bcc*-SI is stable at as low as 20 GPa in excellent agreement with theory [3,25,30] (Supplementary Fig. 2), revealing that the Hugoniot pathway barely misses this phase (Supplementary Fig. 10), while shock compression of even slightly pre-compressed water (1-3 GPa) as in Refs. [19,46] is able to probe and document it by optical conductivity measurements (Supplementary Fig. 10). The low-pressure (<20 GPa) melting and emergence of *bcc*-SI phase agrees with recent XRD observations [34], while the present study is at odds with this and other experiments in that it shows the higher temperature

melt line and the emergence of *fcc*-SI phase above 30 GPa and 1450 K (Supplementary Fig. 1). The discrepancy may be due to difficulties in controlling/measuring temperature and phase composition in the laser heating experiment of Ref. [34] (Supplementary Fig. 15). We speculate that these are related to the optical absorption of SI phases (Fig. 4) blocking thermal radiation from the hottest part of the sample and likely causing laser heating instability effects.

Our XRD results for SI phases extrapolated to higher pressures are consistent with those of laser shock experiments of Ref. [19] (Supplementary Fig. 2) in the location of the melting line near 190 GPa and 5000 K and the stability domain of a SI phase (Supplementary Fig. 10). However, the most recent reverberating shock experiments [33] determined much lower temperatures of stability of the *fcc*-SI state (Supplementary Figs. 2, 10), which are definitely inconsistent with our direct temperature determination. Setting aside possible temperature metrology problems (temperature was determined by model calculations in Ref. [33]), we propose that these nanosecond long experiments have not been able to probe the thermodynamic equilibrium states [48]. The compression pathways of Ref. [33] drive the sample through the stability domain of either *bcc*-SI or *fcc*-SI depending on the strength of initial shock (Supplementary Fig. 10). The sample was probed instantaneously by XRD at the later time (2-5 ns). The *bcc*-SI or *fcc*-SI phases, formed in the initial stage of compression, could remain as metastable phases in the stability field of ice X. We emphasize that our static *in situ* experiments are crucial for understanding the phase diagram of water at extreme P-T conditions.

Our combined XRD and optical spectroscopy experiments establish the existence of P-T domains of stability of two phases, which are inferred to be superionic ices based on the high values of optical conductivity measured here. We have also identified a range of temperatures over which fluid water has high values of optical conductivity. These data allow us to address an important question about a possible contribution of water phases to the generation of the non-dipolar non-axisymmetric magnetic fields of Uranus and Neptune. Numerical dynamo simulations found that the magnetic fields of these planets are generated in a relatively thin and shallow conducting fluid shell (down to one-third of planetary radius) above a stably stratified interior [9,49]. We uphold this view as the P-T boundaries of H_2O phases established here are consistent with fluid water in the upper third of Uranus and Neptune. At greater depths water transitions to a solid *fcc*-SI of H_2O at 56(71) GPa corresponding to 74(67) % of the Uranus (Neptune) planetary radius [50], which may allow for the stably-stratified interior. Future studies addressing the conductivities and viscosity of superionic ices will further our understanding of the interiors of Uranus and Neptune.

Acknowledgments: Porous carbon samples were received from Dr. Maria E. Fortunato and Professor Kenneth S. Suslick, University of Illinois at Urbana-Champaign. We thank Zack Geballe for useful comments on the manuscript. This work was performed at GeoSoilEnviroCARS (The University of Chicago, Sector 13), Advanced Photon Source (APS), and Argonne National Laboratory. We are very thankful to the four anonymous reviewers for helpful suggestion and comments that helped us to improve the manuscript.
Funding: GeoSoilEnviroCARS is supported by the National Science Foundation – Earth Sciences (EAR – 1634415) and Department of Energy- GeoSciences (DE-FG02-94ER14466).

This research used resources of the Advanced Photon Source, a U.S. Department of Energy (DOE) Office of Science User Facility operated for the DOE Office of Science by Argonne National Laboratory under Contract No. DE-AC02-06CH11357. The work at Carnegie was supported by the NSF (Grant Nos. DMR-1039807, EAR/IF-1128867, and EAR-1763287), the Army Research Office (Grant Nos. 56122-CH-H and W911NF1920172), the Deep Carbon Observatory, and the Carnegie Institution of Washington. S.S.L. acknowledges the support of the Helmholtz Young Investigators Group CLEAR (VH-NG-1325).

Author contributions: V.B.P. and A.F.G. conceived the experiments; V.B.P., N.H., S.S.L., and A.F.G. designed the experiments; V.B.P., N.H., and S.S.L. executed the experiments; V.B.P., N.H., and A.F.G. analyzed the data; A.F.G. and V.B.P. wrote the manuscript; and all authors reviewed and discussed the manuscript during preparation.

Competing interests: All authors declare no competing interests.

Data and materials availability: All data are available in the manuscript or the supplementary information.

SUPPLEMENTARY INFORMATION

Supplementary notes

Tables 1-4

Figures 1-18

References (1-29)

FIGURE CAPTIONS

Fig. 1. **Phase diagram of water at extreme P-T conditions.** Solid phases are labeled after Ref. [6]. Fluid phases are labeled following Ref. [35] and the results of this work reporting a conducting fluid. All symbols except cyan circles are the results of this work and show P-T conditions of selected XRD measurements and the onset temperatures for optical absorption. The regions labeled as molecular/ionic and conducting fluids differ by the optical properties measured in this work. Cyan circles show Raman data from Refs. [5,6] (no error bars for clarity) for the phase line between ice VII and dynamically disordered ice VII′. The one-side pressure error bars and filled symbols (skipped for clarity below 1600 K, where the error bars are comparable to the symbol size) correspond to our estimation of the thermal pressure (Supplementary Information, Supplementary Fig. 9). The solid lines (guides to the eye) correspond to the proposed phase lines. The melting line above 60 GPa has a large uncertainty because of deterioration of the temperature control in the regime where water becomes absorptive (Methods). We refer to Supplementary Information Figs. 1, 2 for comparisons with other experiments and theoretical calculations and also for the density-temperature phase diagram. The calculated isentropes of Neptune and Uranus are from Ref. [8].

Figure 2. **XRD patterns measured on laser heating (LH) at 49 GPa (a) and 150 GPa (b).** (The stated pressures are nominal pressures at 300 K labeled as RT). At 49 GPa, *bcc*-SI and *fcc*-SI (the *fcc*-SI peaks are marked by the vertical arrows) phases appear at 1600 and 2000 K, respectively. At 150 GPa, the *fcc*-SI phase appears at 5200 K, and no *bcc*-SI is detected. The

peaks of the low-temperature phases are visible at high temperatures because of the axial temperature gradients. "*St*" stands for stishovite phase of SiO_2 (which was used as the thermal insulator). The transitions are fully reversible, which is seen based on XRD of the quenched to 300 K sample. The ticks correspond to the Bragg reflections of the refined structures, see Supplementary Fig. 6 for the lattice parameters and for the patterns where the peaks of *bcc*-SI phase can be seen clearer. The top inset panels are the XRD images in rectangular coordinates (cake) for 49 GPa and in polar coordinates for 150 GPa. The inset panel in (b) demonstrates diffuse scattering of partially molten water at 5200 K; it is obtained by subtracting the diffraction pattern of the quenched to 300 K sample (raw data). The X-ray wavelength is 0.3344 Å.

Figure 3. **Density vs P for 300 K ices, superionic phases, and fluid water**. The densities of combined ices VII and X at 300 K (crossed-haired blue squares), combined *bcc*-SI (yellow crossed squares) and *fcc*-SI (crossed-haired diamonds) in their P-T stability regions (solid lines), and fluid water at the melting line (red dashed lines approximating the data of Refs. [19,22]) are shown; the details about the parameters of these dependencies presented in the Vinet form are in Supplementary Table 4. The uncertainties of our density experiments are smaller than the symbol size. The one-directional error bars and filled symbols show the uncertainties in thermal pressure measurements of *bcc*-SI and *fcc*-SI (Supplementary Fig. 9). Our data are compared to the results of dynamic experiments of Refs. [19,33]. A detailed comparison of the data with previous experiments and theoretical calculations are shown in the Supplementary Fig. 8.

Figure 4. Optical spectroscopy data of SI phases and fluid water. (a) Optical absorption spectra at various P-T conditions; the error bars represent an uncertainty in the optical signal intensity; the solid lines are guides to the eye. (b) Optical conductivity determined here using a broadband spectroscopy in comparison with the results at 532 nm of Ref. [19] obtained along the Hugoniot. The solid lines are guides to the eye. The sample thickness was determined approximately using the finite element calculations (see Methods and Supplementary Figs. 15-16 for more detailed information). The error bars for the conductivity values in (b) reflect this uncertainty.

References and Notes:

1 Goncharov, A. F., Struzhkin, V. V., Somayazulu, M. S., Hemley, R. J. & Mao, H. K. Compression of Ice to 210 Gigapascals: Infrared Evidence for a Symmetric Hydrogen-Bonded Phase. *Science* **273**, 218-220, doi:10.1126/science.273.5272.218 (1996).

2 Benoit, M., Marx, D. & Parrinello, M. Tunnelling and zero-point motion in high-pressure ice. *Nature* **392**, 258, doi:10.1038/32609 (1998).

3 Cavazzoni, C. *et al.* Superionic and Metallic States of Water and Ammonia at Giant Planet Conditions. *Science* **283**, 44-46, doi:10.1126/science.283.5398.44 (1999).

4 Benoit, M., Romero, A. H. & Marx, D. Reassigning Hydrogen-Bond Centering in Dense Ice. *Physical Review Letters* **89**, 145501, doi:10.1103/PhysRevLett.89.145501 (2002).

5 Goncharov, A. F. *et al.* Dynamic Ionization of Water under Extreme Conditions. *Physical Review Letters* **94**, 125508, doi:10.1103/PhysRevLett.94.125508 (2005).

6 Goncharov, A. F. & Crowhurst, J. Proton delocalization under extreme conditions of high pressure and temperature. *Phase Transitions* **80**, 1051-1072, doi:10.1080/01411590701473101 (2007).
7 Holzapfel, W. B. Symmetry of hydrogen bonds in ice -VII *Journal of Chemical Physics* **56**, 712-715, doi:10.1063/1.1677221 (1972).
8 Redmer, R., Mattsson, T. R., Nettelmann, N. & French, M. The phase diagram of water and the magnetic fields of Uranus and Neptune. *Icarus* **211**, 798-803, doi:https://doi.org/10.1016/j.icarus.2010.08.008 (2011).
9 Stanley, S. & Bloxham, J. Convective-region geometry as the cause of Uranus' and Neptune's unusual magnetic fields. *Nature* **428**, 151-153 (2004).
10 Schwager, B., Chudinovskikh, L., Gavriliuk, A. & Boehler, R. Melting curve of H_2O to 90 GPa measured in a laser-heated diamond cell. *Journal of Physics: Condensed Matter* **16**, S1177, doi:10.1088/0953-8984/16/14/028 (2004).
11 Lin, J.-F. *et al.* High pressure-temperature Raman measurements of H2O melting to 22 GPa and 900 K. *The Journal of Chemical Physics* **121**, 8423-8427, doi:10.1063/1.1784438 (2004).
12 Schwager, B. & Boehler, R. H_2O: another ice phase and its melting curve. *High Pressure Research* **28**, 431-433, doi:10.1080/08957950802347973 (2008).
13 Ahart, M., Karandikar, A., Gramsch, S., Boehler, R. & Hemley, R. J. High P–T Brillouin scattering study of H_2O melting to 26 GPa. *High Pressure Research* **34**, 327-336, doi:10.1080/08957959.2014.946504 (2014).
14 Frank, M. R., Fei, Y. & Hu, J. Constraining the equation of state of fluid H_2O to 80 GPa using the melting curve, bulk modulus, and thermal expansivity of Ice VII *Geochimica et Cosmochimica Acta* **68**, 2781-2790, doi:doi.org/10.1016/j.gca.2003.12.007 (2004).
15 Dubrovinsky, L. & Dubrovinskaia, N. in *Advances in High-Pressure Mineralogy* (ed Eiji Ohtani) (Geological Society of America, 2007).
16 Datchi, F., Loubeyre, P. & LeToullec, R. Extended and accurate determination of the melting curves of argon, helium, ice H_2O, and hydrogen H_2. *Physical Review B* **61**, 6535-6546, doi:10.1103/PhysRevB.61.6535 (2000).
17 Lin, J.-F. *et al.* Melting behavior of H_2O at high pressures and temperatures. *Geophysical Research Letters* **32**, doi:10.1029/2005GL022499 (2005).
18 Kimura, T., Kuwayama, Y. & Yagi, T. Melting temperatures of H_2O up to 72 GPa measured in a diamond anvil cell using CO2 laser heating technique. *The Journal of Chemical Physics* **140**, 074501, doi:10.1063/1.4865252 (2014).
19 Millot, M. *et al.* Experimental evidence for superionic water ice using shock compression. *Nature Physics* **14**, 297-302, doi:10.1038/s41567-017-0017-4 (2018).
20 Méndez, A. S. J. *et al.* Bulk modulus of H_2O across the ice VII-ice X transition measured by time-resolved x-ray diffraction in dynamic diamond anvil cell experiments. *Physical Review B* **103**, 064104, doi:10.1103/PhysRevB.103.064104 (2021).
21 Schwegler, E., Sharma, M., Gygi, F. & Galli, G. Melting of ice under pressure. *Proceedings of the National Academy of Sciences* **105**, 14779, doi:10.1073/pnas.0808137105 (2008).
22 Goncharov, A. F. *et al.* Dissociative melting of ice VII at high pressure. *The Journal of Chemical Physics* **130**, 124514, doi:10.1063/1.3100771 (2009).
23 Sugimura, E. *et al.* Experimental evidence of superionic conduction in H_2O ice. *The Journal of Chemical Physics* **137**, 194505, doi:10.1063/1.4766816 (2012).

24 Aragones, J. L. & Vega, C. Plastic crystal phases of simple water models. *The Journal of Chemical Physics* **130**, 244504, doi:10.1063/1.3156856 (2009).
25 Hernandez, J.-A. & Caracas, R. Superionic-Superionic Phase Transitions in Body-Centered Cubic H_2O Ice. *Physical Review Letters* **117**, 135503, doi:10.1103/PhysRevLett.117.135503 (2016).
26 Hernandez, J.-A. & Caracas, R. Proton dynamics and the phase diagram of dense water ice. *The Journal of Chemical Physics* **148**, 214501, doi:10.1063/1.5028389 (2018).
27 French, M., Mattsson, T. R., Nettelmann, N. & Redmer, R. Equation of state and phase diagram of water at ultrahigh pressures as in planetary interiors. *Physical Review B* **79**, 054107, doi:10.1103/PhysRevB.79.054107 (2009).
28 Goldman, N., Fried, L. E., Kuo, I. F. W. & Mundy, C. J. Bonding in the Superionic Phase of Water. *Physical Review Letters* **94**, 217801, doi:10.1103/PhysRevLett.94.217801 (2005).
29 Mattsson, T. R. & Desjarlais, M. P. Phase Diagram and Electrical Conductivity of High Energy-Density Water from Density Functional Theory. *Physical Review Letters* **97**, 017801, doi:10.1103/PhysRevLett.97.017801 (2006).
30 French, M., Desjarlais, M. P. & Redmer, R. Ab initio calculation of thermodynamic potentials and entropies for superionic water. *Physical Review E* **93**, 022140, doi:10.1103/PhysRevE.93.022140 (2016).
31 Wilson, H. F., Wong, M. L. & Militzer, B. Superionic to Superionic Phase Change in Water: Consequences for the Interiors of Uranus and Neptune. *Physical Review Letters* **110**, 151102, doi:10.1103/PhysRevLett.110.151102 (2013).
32 Sun, J., Clark, B. K., Torquato, S. & Car, R. The phase diagram of high-pressure superionic ice. *Nature Communications* **6**, 8156, doi:10.1038/ncomms9156 (2015).
33 Millot, M. *et al.* Nanosecond X-ray diffraction of shock-compressed superionic water ice. *Nature* **569**, 251-255, doi:10.1038/s41586-019-1114-6 (2019).
34 Queyroux, J. A. *et al.* Melting Curve and Isostructural Solid Transition in Superionic Ice. *Physical Review Letters* **125**, 195501, doi:10.1103/PhysRevLett.125.195501 (2020).
35 Rozsa, V., Pan, D., Giberti, F. & Galli, G. Ab initio spectroscopy and ionic conductivity of water under Earth mantle conditions. *Proceedings of the National Academy of Sciences* **115**, 6952-6957, doi:10.1073/pnas.1800123115 (2018).
36 Ninet, S., Datchi, F. & Saitta, A. M. Proton Disorder and Superionicity in Hot Dense Ammonia Ice. *Physical Review Letters* **108**, 165702, doi:10.1103/PhysRevLett.108.165702 (2012).
37 McWilliams, R. S., Dalton, D. A., Mahmood, M. F. & Goncharov, A. F. Optical Properties of Fluid Hydrogen at the Transition to a Conducting State. *Physical Review Letters* **116**, 255501 (2016).
38 Jiang, S. *et al.* Metallization and molecular dissociation of dense fluid nitrogen. *Nature Communications* **9**, 2624, doi:10.1038/s41467-018-05011-z (2018).
39 Zhang, M., Putnis, A. & Salje, E. K. H. Infrared spectroscopy of superionic conductor LiNaSO4: Vibrational modes and thermodynamics. *Solid State Ionics* **177**, 37-43, doi:https://doi.org/10.1016/j.ssi.2005.10.001 (2006).
40 Li, J. *et al.* Electronic bandgap of water in the superionic and plasma phases. *Physics of Plasmas* **26**, 092703, doi:10.1063/1.5110544 (2019).
41 Sun, J. *High Pressure Superionic Ice Phase Diagram* DOCTOR OF PHILOSOPHY thesis, Princeton, (2019).

42 French, M., Mattsson, T. R. & Redmer, R. Diffusion and electrical conductivity in water at ultrahigh pressures. *Physical Review B* **82**, 174108, doi:10.1103/PhysRevB.82.174108 (2010).
43 Mitchell, A. C. & Nellis, W. J. Equation of state and electrical conductivity of water and ammonia shocked to the 100 GPa (1 Mbar) pressure range. *The Journal of Chemical Physics* **76**, 6273-6281, doi:10.1063/1.443030 (1982).
44 Yakushev, V. V., Postnov, V. I., Fortov, V. E. & Yakysheva, T. I. Electrical conductivity of water during quasi-isentropic compression to 130 GPa. *Journal of Experimental and Theoretical Physics* **90**, 617-622, doi:10.1134/1.559145 (2000).
45 Chau, R., Mitchell, A. C., Minich, R. W. & Nellis, W. J. Electrical conductivity of water compressed dynamically to pressures of 70–180 GPa (0.7–1.8 Mbar). *The Journal of Chemical Physics* **114**, 1361-1365, doi:10.1063/1.1332079 (2001).
46 Lee, K. K. M. *et al.* Laser-driven shock experiments on precompressed water: Implications for "icy" giant planets. *The Journal of Chemical Physics* **125**, 014701, doi:10.1063/1.2207618 (2006).
47 McWilliams, R. S., Dalton, D. A., Konôpková, Z., Mahmood, M. F. & Goncharov, A. F. Opacity and conductivity measurements in noble gases at conditions of planetary and stellar interiors. *Proceedings of the National Academy of Sciences of the United States of America* **112**, 7925-7930 (2015).
48 Duffy, T. S. & Smith, R. F. Ultra-High Pressure Dynamic Compression of Geological Materials. *Frontiers in Earth Science* **7**, doi:10.3389/feart.2019.00023 (2019).
49 Gómez-Pérez, N. & Heimpel, M. Numerical models of zonal flow dynamos: an application to the ice giants. *Geophysical & Astrophysical Fluid Dynamics* **101**, 371-388, doi:10.1080/03091920701485537 (2007).
50 Helled, R., Anderson, J. D., Podolak, M. & Schubert, G. Interior Models of Uranus and Neptune. *The Astrophysical Journal* **726**, 15, doi:10.1088/0004-637x/726/1/15 (2010).

Methods

X-ray diffraction (XRD) combined with laser heating (LH) experiment

We have used standard symmetric and mini BX-90 diamond anvil cells (DACs) [51]. In most of the experiments, we used cBN X-ray transparent diamond anvil seats to maximize the X-ray opening up to $2\theta=20°$ thus enabling observations of higher order Bragg reflections of SI ices (Supplementary Fig. 6). Diamond anvils with flat culet size of 300 μm and 250 μm and beveled culets 150/300 μm (8 degrees) were used to generate pressure up to 70, 110, and 150 GPa, respectively. Typical size of the pressure chamber was 60-100 μm in diameter drilled in a Re gasket pre-indented to 25-35 μm thickness. Various combinations of the water sample with laser absorbers (couplers) and insulating layers were used to minimize the axial temperature gradients across the probed sample region and to avoid possible chemistry effects (Supplementary Table 1). Only high purity H_2O water (18 Ω) was used as a sample. For XRD measurements, we found that the optimal configuration for laser heating experiments on H_2O ice is when SiO_2 was used as the anvil insulating layer and porous carbon as the laser absorber (Supplementary Fig. 18); small flakes of gold (including particles of 0.5-1.0 μm sizes) were used in all experiments for pressure determination and in some experiments (especially above 100 GPa) as the laser coupler (if detached from the anvils). Other coupler and thermal insulation materials (Supplementary Table 1) have been used to test that the use of these materials does not affect the reported here transition in ice. For the results reported here using carbon and Au as the couplers and Al_2O_3 and SiO_2 as the thermal insulation, we find that except occasional diamond formation (from porous carbon) and minor hydrolyzation of Al_2O_3 [52] and SiO_2 [53] no irreversible phase transformations or chemical reaction have been detected with XRD and Raman spectroscopy performed on the quenched to room temperature samples making our laser heating measurements suitable for *in situ* high-temperature probes of ice and water at extreme P-T conditions. The presence of additional materials in the DAC chamber did not adversely affect the stress conditions in the DAC chamber. Indeed, after the first laser heating Bragg peaks of ice become sharp and their positions indicate substantially reduced nonhydrostatic stresses.

All diffraction experiments were conducted at the GSECARS undulator beamline (sector 13, APS, ANL) with X-ray beam focused down to a less than 3x4 μm^2 spot with the energy of 37.07 keV and 40.0 keV (Supplementary Fig. 18). MAR-165 CCD was used to collect high resolution XRD with exposure time varied from 5 to 60 s. The detector position and geometry were calibrated with CeO_2 and LaB_6 NIST standards. XRD measurements were combined with double-sided flat-top coaxial near IR (1064 nm) laser heating [54] that was used in all experiments except one experiment where one-side heating with a CO_2 laser was utilized. The laser heating flat top focal spot was about 10 μm in diameter which is much larger than the X-ray beam spot to reduce the temperature gradients across the probed part of the sample and to enable the use of the internal heat absorber (coupler). The sample temperature was controlled in a wide range via the variation of the laser power in continuous wave (CW) or flash (quasi-continuous, 5 s or longer) modes. The sample temperature was measured radiometrically (gray body approximation)

concomitantly with the XRD measurements; several measurements were normally taken sequentially from both sides of the sample to insure a uniform and stable in time heating, which was maintained within ±5% of the nominal temperature value (Supplementary Fig. 14). The thermal radiation was recorded with a Princeton grating spectrometer (300 mm focal length) combined with PIXIS and PiMAx CCD array detectors. The system optical response was calibrated with the NIST certified tungsten lamp [55], and the literature data for the melting temperature of graphite and Pt at ambient pressure were reproduced. For precise alignment of laser heating and optical measurements paths we used an x-ray induced fluorescence spot on sample from both sides of the system [54]. The statistical errors of radiative T measurements are rather small (Supplementary Fig. 14) because of the high throughput of the optical system; however larger systematic errors due to the gray body approximation and chromatic aberrations are possible [55,56]. According to Ref. 55, which is specific for the beamline used in this work, the errors originated from chromatic aberration are essentially eliminated by the spectral intensity calibration as long as the heating spot is uniform. This was the case in this work where the samples were heated uniformly using flat top laser heating. The uncertainties due to a variable thermal emissivity (Ref. 56) have been determined to be of the order of several hundred Kelvins depending on the optical properties of the sample. These errors as well as those related to deterioration of the temperature control due to water absorption and associated temperature runaway (see below) dominate in our estimation of the radiative temperature uncertainties (Fig. 1). For the data reduction we used Dioptas, T-Rax, LightField® and Jade software packages [57-60].

In this study, more than 5900 unique XRD patterns were collected at hundreds pressure-temperature conditions. For each DAC loading, we have performed laser heating runs to various temperatures at a number of selected pressure points. The summary of all the sample configurations used and P-T conditions probed in this work are listed in the Supplementary Table 1. The data selected for the determination of the phase diagram shown in Fig. 1 and the Equations of State (EOS) in Fig. 3 were collected in laser heating experiments, which demonstrated reversibility to an initial state (*e.g.* ice VII) after quenching down to room temperature (Supplementary Figs. 3, 5). Moreover, most of them are the result of multiple runs at similar P-T conditions. Only near IR laser heating experiments are reported here. CO_2 laser heating (10.6 μm laser wavelength), external heating, and cryo-cooling experiments yielded the results consistent with near IR laser heating experiments (in a common P-T domain) and are not presented here.

Our experiments do not show any effect of insulating layer or laser absorber material types on the P-T conditions of emergence and the structural properties of superionic phases of H_2O. In the most H_2O melting experiments, hydrolyzation of insulating layer (SiO_2, Al_2O_3 [52,53]) was observed while no change in the sample properties and phase states was detected. Very large temperature gradients across insulating layers results in non-uniform hydrolyzation that prevents definitive characterization of formed hydrous phases.

No insulation was used above 100 GPa. Because of this and a greatly reduced high-pressure cavity thickness between the diamond anvils working as heat sinks, the temperature gradients across the sample (heated indirectly via an absorber) become very large at high pressures; this results in observations of phase mixtures, especially at high pressures as shown in Fig. 2, and Supplementary Figs. 3-6. However, our finite element calculations [61] show that in the case of

internal coupler (modelled here as a metal foil with a cylindrical hole or volumetrically uniformly absorbing coupler filling the whole or the central part of the cavity such as porous carbon or gold nanoparticles) the temperature gradients are moderate near the laser heated spot (Supplementary Fig. 15). The temperature map across the cavity has a broad region where it changes moderately (~10%) near the center of the cavity and the temperature drops sharply toward the anvils in the axial direction and away from the heating spot in the radial direction outside of x-ray probed area. Accordingly, the XRD signal from the central region is only weakly distorted by relatively small temperature gradients near the center of the cavity. The regions closer to the anvils with a large temperature gradient also contribute to the overall XRD signal and yield the signal corresponding to parts of the sample with lower temperatures; this can be additionally affected by deviatoric stresses due to the emergence of SI phases with larger specific volumes in the hot zone in the middle of the cavity. However, given the typical temperature distributions in our experiments (Supplementary Fig. 15), one cannot expect a bimodal XRD peak shape originated from the same uninterrupted in space ice phase because of the thermal expansion (*e.g*. Ref. [62]). Thus, the observations of distinct XRD peaks of *bcc*-SI with the larger d-spacings than of *bcc* ices VII, VII', and X signify the existence of this phase. The presence of thin thermal insulation layers on both diamond anvils (used below 100 GPa) diminishes the signal of spurious phases at close to room temperature conditions (*e.g*. of ice VII) (Supplementary Fig. 6).

Upon temperature increase, SI ices and fluid water become more light absorbing (*e.g*. Ref. [46] and Fig. 4), which results in a change in the laser energy transfer pattern to the sample. This results in deterioration of the temperature controls upon the transition to *bcc*-SI and *fcc*-SI phases and fluid states, because of an increased laser absorption in these states; this produces a runaway increase of temperature while laser power is gradually increased. Also, the apparent recorded temperature, which can be affected by the sample absorption blocking or modifying the spectrum of the thermal radiation from the hottest parts of the sample [63], can be different from the top temperature of the sample. However, this effect, which can cause errors up to 500 K in extreme cases [64] is small here because the absorption spectra of water and SI phases are rather wavelength independent (Fig. 4), while the temperature has a plateau near the laser heated spot in the middle of the cavity (Supplementary Fig. 15). The temperature redistribution due to the H_2O sample absorption can cause temperature instabilities and fluctuations and, thus, large uncertainties in the radiative temperature measurements as reflected in increased error bars (Fig. 1). To mitigate these effects we used flash (in XRD experiments) or pulsed (in optical experiments as described below) laser heating techniques where each heating event comprises simultaneous collection of XRD or optical properties, respectively, and radiometric temperature measurements as described here.

Pressure in XRD experiments was measured at room temperature using a variety of gauges such as ruby, Raman of the stressed diamond [65], and XRD of Au (bulk) [66], SiO_2 [67], and Al_2O_3 [68]. An example of XRD measurements of the lattice parameters of ices and thermal insulation upon laser heating at the nominal pressure of 21 GPa is presented in the Supplementary Table 2 and Supplementary Fig. 9. Pressure determination in laser heated DAC at high T is a long-standing and yet unresolved challenge [69,70]. Such determination requires careful combined measurements

of the sample and a pressure gauge, positioned in a close proximity and experiencing similar stresses and temperature; this is complex and unreliable (thermal pressure changes very rapidly in the hot spot). This problem becomes even more complex in the case of several phases with different physical properties (e.g. SI) presented in the same high-pressure cavity. Alternatively, one can use various approximation to estimate the thermal pressure based on thermodynamic properties of the sample and surrounding materials. In this work, no apparent correction for the thermal pressure at high temperature has been made, because of the uncertainties in its determination related to the unknown thermal EOS of the common high-density ices at high P-T conditions and the phase transitions (*e.g.* to SI phases), which change the sample specific volume (Fig. 3). We estimated the thermal pressure in our experiments utilizing previously measured thermal EOS of ice VII (VII′) below 80 GPa and 900 K [14] and extrapolating it to higher P-T conditions (Supplementary Fig. 9). This yielded moderate values for the thermal pressure (*e.g.* 12 GPa at 3220 K and 124 GPa), which are substantially smaller than expected for isochoric heating; this behavior is common for laser heating in DAC (*e.g.* Ref. [71]). These rather moderate values are also in a qualitative agreement with the theoretically calculated thermal expansion of ice and its superionic modifications (Supplementary Fig. 9)

Optical spectroscopy measurements combined with laser heating experiment

To assess the optical conductivity of water at extreme P-T conditions, we exploited time domain optical transmission measurements using pulsed laser heating in the DAC similar to those described in our previous publications (Supplementary Fig. 17) [37,38,47,72]. Our experiments combine optical emission and transmission spectroscopy measurements in the visible spectral range (480–750 nm) using a streak camera coupled to a single grating spectrometer; we used a grating with 75 gr/mm covering the whole visible spectral range, thus eliminating the necessity to stitch spectra measured at different spectral positions. Fluid water was loaded in a high-pressure cavity along with a metallic (Ir) suspended (tested using Raman spectroscopy of water after the loading) foil (coupler) of 2-8 μm thickness (depending on the final P range), which has one or several cylindrical holes of 6–8 μm in diameter. Water was conductively heated in a hole of the coupler by a fiber laser (1064 nm) heating the surrounding coupler rim (Supplementary Fig. 15). The sample was heated with laser pulses of 4–10 μs duration; FE model calculations [37,38,61] (Supplementary Fig. 16) have been used to model the temperature distribution in the high-pressure cavity. The temperature gradients are very sharp in the initial stage of heating when the first sharp laser heating pulse is absorbed but over a few μs, the temperature gradients become much shallower (Supplementary Fig. 16) and the temperature map at the time corresponding to the maximum temperature in the center of the sample is very similar to that calculated for continuous heating (Supplementary Fig. 15). This arrangement holds upon cooling thus allowing us to take optical measurements as a function of temperature, which is measured concomitantly radiometrically and can be extrapolated to lower temperatures than the detection limit (3000 K here) for spectroradiometry as has been done for the absorptive superionic states (Fig. 1**,** Supplementary Fig. 13).

Our time-domain optical spectroscopy probes of the laser heated samples combined time resolved spectroradiometry and transient transmittance measurements in a confocal geometry suppressing spurious signals (Supplementary Fig. 17). A pulsed broadband supercontinuum (1

MHz, 1 ns, 400–2400 nm) laser having a focal spot of approximately 6 μm was used as the light source for transient transmission measurements. These experiments were performed in a single laser heating event mode where the streak camera captured the spectrograms (Supplementary Figure 13), which comprise time dependent transmission and thermal radiation spectra in a time window (<30 μs) following the arrival of one laser heating pulse. Radiative temperature measurements often require longer collection times to achieve a desired signal-to-noise ratio in the thermal radiation spectra, which was realized by averaging several (5-20) heating events using the identical laser heating power while no supercontinuum laser probe was applied to avoid ripples in the thermal radiation spectra. The spectra were fitted to a Planck function (Supplementary Fig. 13) to extract the time dependent temperature (with <1 μs time resolution). The detected thermal radiation has contributions from the coupler and the sample. The coupler's temperature is higher than of the sample on heating but they thermalize on cooling, where the measurements of SI phases were taken (Supplementary Fig. 16). The laser heated emitting sample is surrounded by nonabsorptive ices, so the thermal radiation is not expected to be spectrally altered or blocked. The sample temperature was changed by controlling the laser power via laser polarization rotation as described before (*e.g.* Ref. [47]). Several heating experiments were normally performed at the same power level, where the most informative spectrograms were recorded such as in the Supplementary Fig. 13, to ensure the data reproducibility. We determined pressure at room temperature from the spectral position of Raman signal of the stressed diamond anvil near the edge; we find that the pressure readings before and after heating were within 3 GPa. The pressure at high temperature was not measured; the uncertainty in its value due to a thermal pressure at high temperatures was estimated using the thermal equation of state of ice (Supplementary Fig. 9).

The transient absorption coefficient $\alpha=1/d*\ln(I_0/I)$ (d- is the sample thickness) of conducting water at extreme P–T conditions was determined by monitoring the wavelength dependent sample transmission I. The reference transmission spectrum (I_0) was measured at room temperature. This has been measured before each temperature run without laser heating using the same streak camera and spectrograph settings. (A spectrogram measured after the laser shot would normally yield the consistent data unless the diamonds fail of laser coupler moves during/after the heating). This reference spectrogram, which consists of equidistant in time straight lines aligned along the spectral direction (Supplementary Fig. 13 provides examples of spectrograms measured at high temperatures, which document the time and wavelength dependent sample transmission I) has been used to perform the spatial (to correct the line curvature) and the spectral (to normalize the spectra) corrections for the spectrograms measured at extreme P-T conditions. The thickness of SI phase was estimated based on FE calculations of the temperature map as shown in Supplementary Figs. 15-16 (essentially the coupler thickness). We estimated the wavelength dependent optical conductivity of heated water and ices as $\sigma=n\alpha c$, where n- is the refractive index (room-temperature data of Ref. [73] were used), α– is the absorption coefficient, c- is the speed of light, by measuring the temperature dependent attenuation of a pulsed white light (supercontinuum) laser.

Data availability. The data that support the plots within this paper and other findings of this study are available from the corresponding author upon reasonable request.

References and Notes:

51 Kantor, I. *et al.* BX90: A new diamond anvil cell design for X-ray diffraction and optical measurements. *Review of Scientific Instruments* **83**, 125102, doi:10.1063/1.4768541 (2012).

52 Duan, Y. *et al.* Phase stability and thermal equation of state of δ-AlOOH: Implication for water transportation to the Deep Lower Mantle. *Earth and Planetary Science Letters* **494**, 92-98, doi:https://doi.org/10.1016/j.epsl.2018.05.003 (2018).

53 Nisr, C. *et al.* Large H_2O solubility in dense silica and its implications for the interiors of water-rich planets. *Proceedings of the National Academy of Sciences* **117**, 9747-9754, doi:10.1073/pnas.1917448117 (2020).

54 Prakapenka, V. B. *et al.* Advanced flat top laser heating system for high pressure research at GSECARS: application to the melting behavior of germanium. *High Pressure Research* **28**, 225-235, doi:10.1080/08957950802050718 (2008).

55 Shen, G., Rivers, M. L., Wang, Y. & Sutton, S. R. Laser heated diamond cell system at the Advanced Photon Source for in situ x-ray measurements at high pressure and temperature. *Review of Scientific Instruments* **72**, 1273-1282, doi:10.1063/1.1343867 (2001).

56 Benedetti, L. R. & Loubeyre, P. Temperature gradients, wavelength-dependent emissivity, and accuracy of high and very-high temperatures measured in the laser-heated diamond cell. *High Pressure Research* **24**, 423-445, doi:10.1080/08957950412331331718 (2004).

57 Prescher, C. & Prakapenka, V. B. DIOPTAS: a program for reduction of two-dimensional X-ray diffraction data and data exploration. *High Pressure Research* **35**, 223-230, doi:10.1080/08957959.2015.1059835 (2015).

58 Holtgrewe, N., Greenberg, E., Prescher, C., Prakapenka, V. B. & Goncharov, A. F. Advanced integrated optical spectroscopy system for diamond anvil cell studies at GSECARS. *High Pressure Research* **39**, 457-470, doi:10.1080/08957959.2019.1647536 (2019).

59 (Teledyne Princeton Instruments, https://www.princetoninstruments.com/products/software-family/lightfield).

60 (Materials Data, https://materialsdata.com/prodjd.html).

61 Montoya, J. A. & Goncharov, A. F. Finite element calculations of the time dependent thermal fluxes in the laser-heated diamond anvil cell. *Journal of Applied Physics* **111**, 112617 (2012).

62 Panero, W. R. & Jeanloz, R. X-ray diffraction patterns from samples in the laser-heated diamond anvil cell. *Journal of Applied Physics* **91**, 2769-2778, doi:10.1063/1.1435837 (2002).

63 Deng, J., Du, Z., Benedetti, L. R. & Lee, K. K. M. The influence of wavelength-dependent absorption and temperature gradients on temperature determination in laser-heated diamond-anvil cells. *Journal of Applied Physics* **121**, 025901, doi:10.1063/1.4973344 (2017).

64 Lobanov, S. S. & Speziale, S. Radiometric Temperature Measurements in Nongray Ferropericlase With Pressure- Spin- and Temperature-Dependent Optical Properties.

Journal of Geophysical Research: Solid Earth **124**, 12825-12836, doi:10.1029/2019jb018668 (2019).

65 Akahama, Y. & Kawamura, H. Pressure calibration of diamond anvil Raman gauge to 310GPa. *Journal of Applied Physics* **100**, 043516 (2006).

66 Fei, Y. *et al.* Toward an internally consistent pressure scale. *Proceedings of the National Academy of Sciences* **104**, 9182-9186, doi:10.1073/pnas.0609013104 (2007).

67 Fischer, R. A. *et al.* Equations of state and phase boundary for stishovite and CaCl2-type SiO2. *American Mineralogist* **103**, 792-802, doi:10.2138/am-2018-6267 (2018).

68 Dewaele, A. & Torrent, M. Equation of state of Al_2O_3. *Physical Review B* **88**, 064107, doi:10.1103/PhysRevB.88.064107 (2013).

69 Yen, C. E., Williams, Q. & Kunz, M. Thermal Pressure in the Laser-Heated Diamond Anvil Cell: A Quantitative Study and Implications for the Density Versus Mineralogy Correlation of the Mantle. *Journal of Geophysical Research: Solid Earth* **125**, e2020JB020006, doi:https://doi.org/10.1029/2020JB020006 (2020).

70 Anzellini, S. & Boccato, S. A Practical Review of the Laser-Heated Diamond Anvil Cell for University Laboratories and Synchrotron Applications. *Crystals* **10**, doi:10.3390/cryst10060459 (2020).

71 Dewaele, A., Fiquet, G. & Gillet, P. Temperature and pressure distribution in the laser-heated diamond–anvil cell. *Review of Scientific Instruments* **69**, 2421-2426, doi:10.1063/1.1148970 (1998).

72 Jiang, S. *et al.* A Spectroscopic Study of the Insulator–Metal Transition in Liquid Hydrogen and Deuterium. *Advanced Science* **7**, 1901668, doi:10.1002/advs.201901668 (2020).

73 Zha, C.-S., Hemley, R. J., Gramsch, S. A., Mao, H.-k. & Bassett, W. A. Optical study of H_2O ice to 120GPa: Dielectric function, molecular polarizability, and equation of state. *The Journal of Chemical Physics* **126**, 074506, doi:10.1063/1.2463773 (2007).

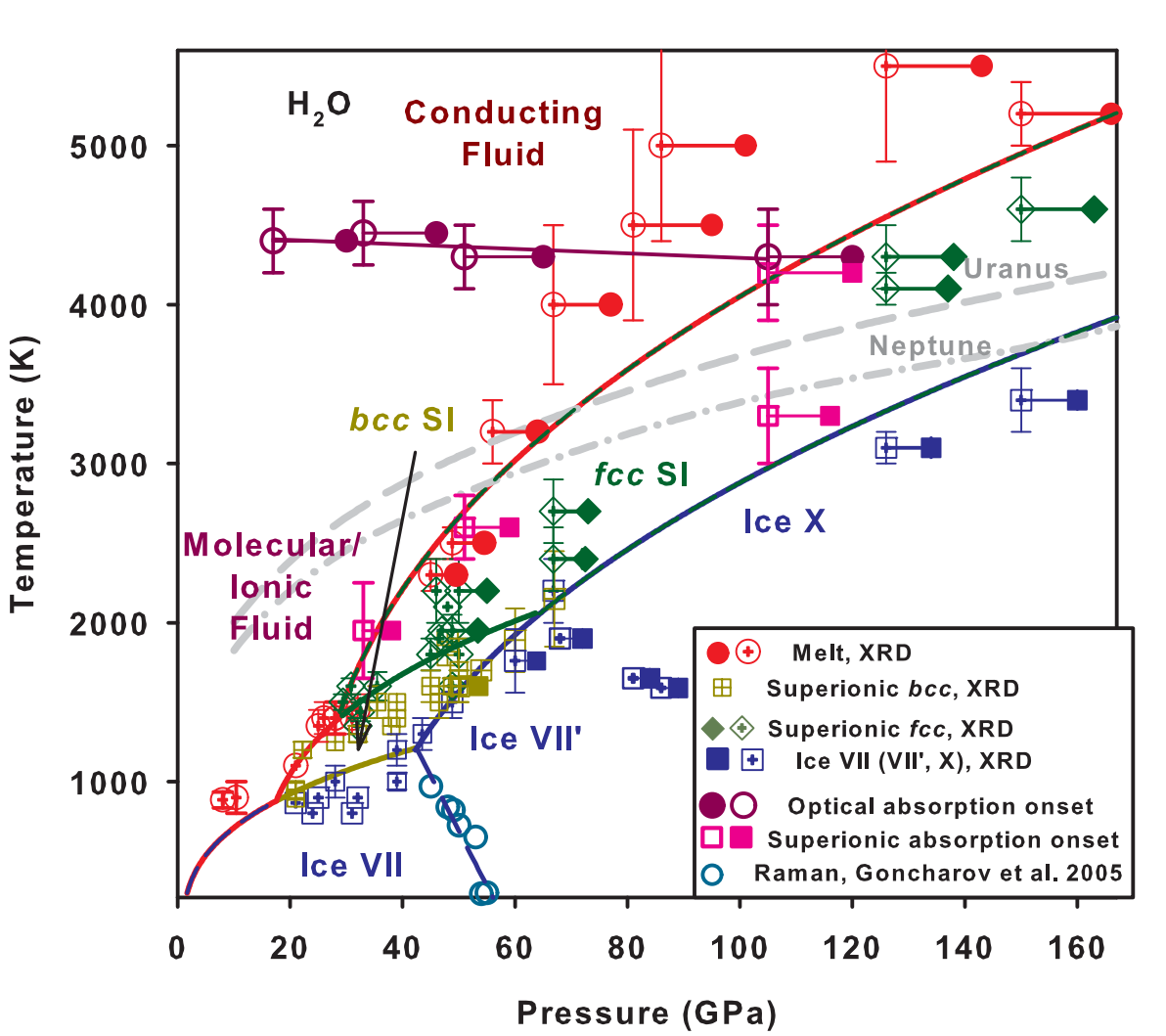
H2O
Conducting Fluid
Uranus
Neptune
bcc SI
fcc SI
Ice X
Molecular/ Ionic Fluid
Ice VII'
Ice VII
Melt, XRD
Superionic bcc, XRD
Superionic fcc, XRD
Ice VII (VII', X), XRD
Optical absorption onset
Superionic absorption onset
Raman, Goncharov et al. 2005
Temperature (K)
Pressure (GPa)
1000
2000
3000
4000
5000
0
20
40
60
80
100
120
140
160

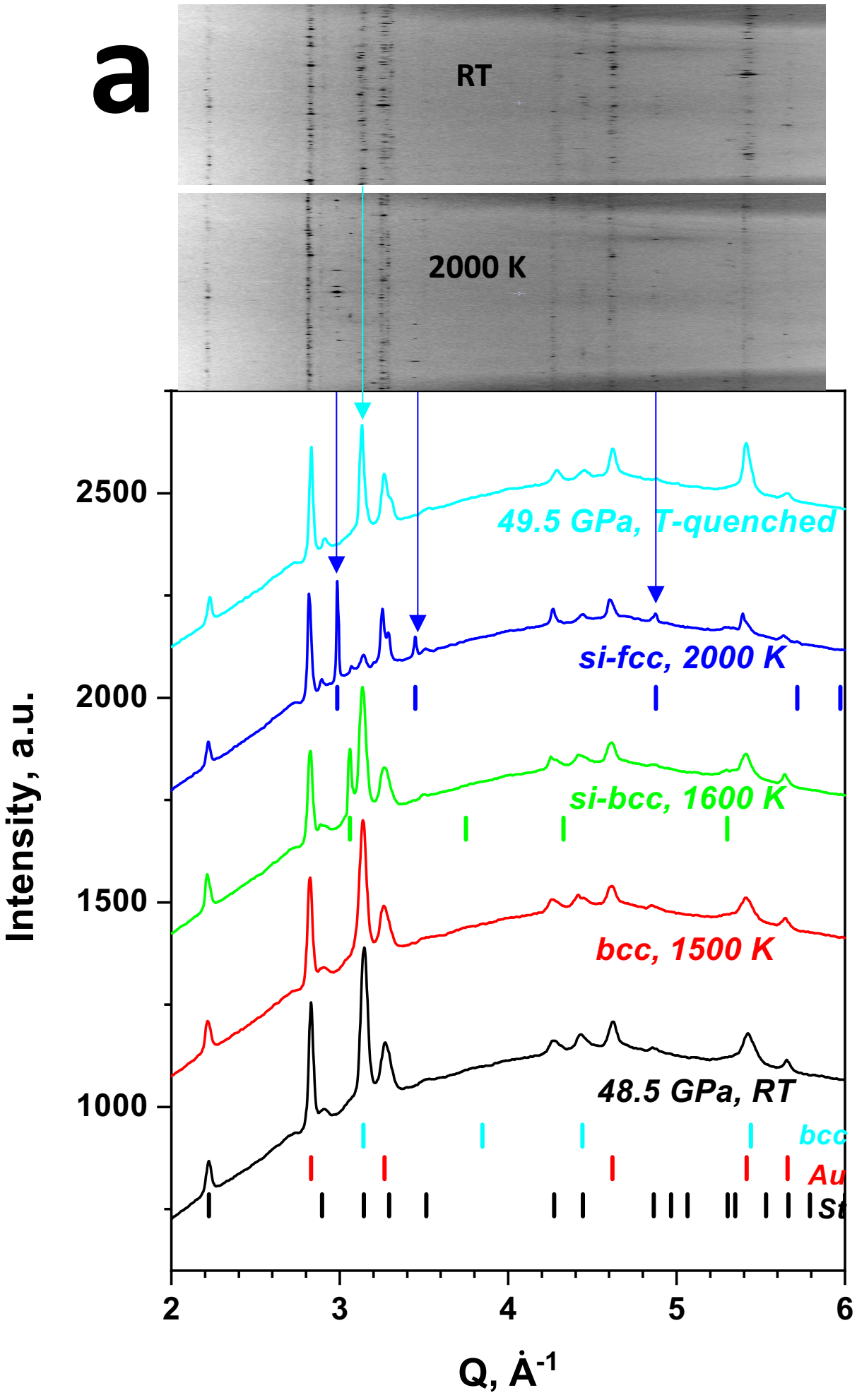
a
RT
2000 K
2500
2000
1500
1000
Intensity, a.u.
49.5 GPa, T-quenched
si-fcc, 2000 K
si-bcc, 1600 K
bcc, 1500 K
48.5 GPa, RT
bcc
Au
St
2
3
4
5
6
Q, Å-1

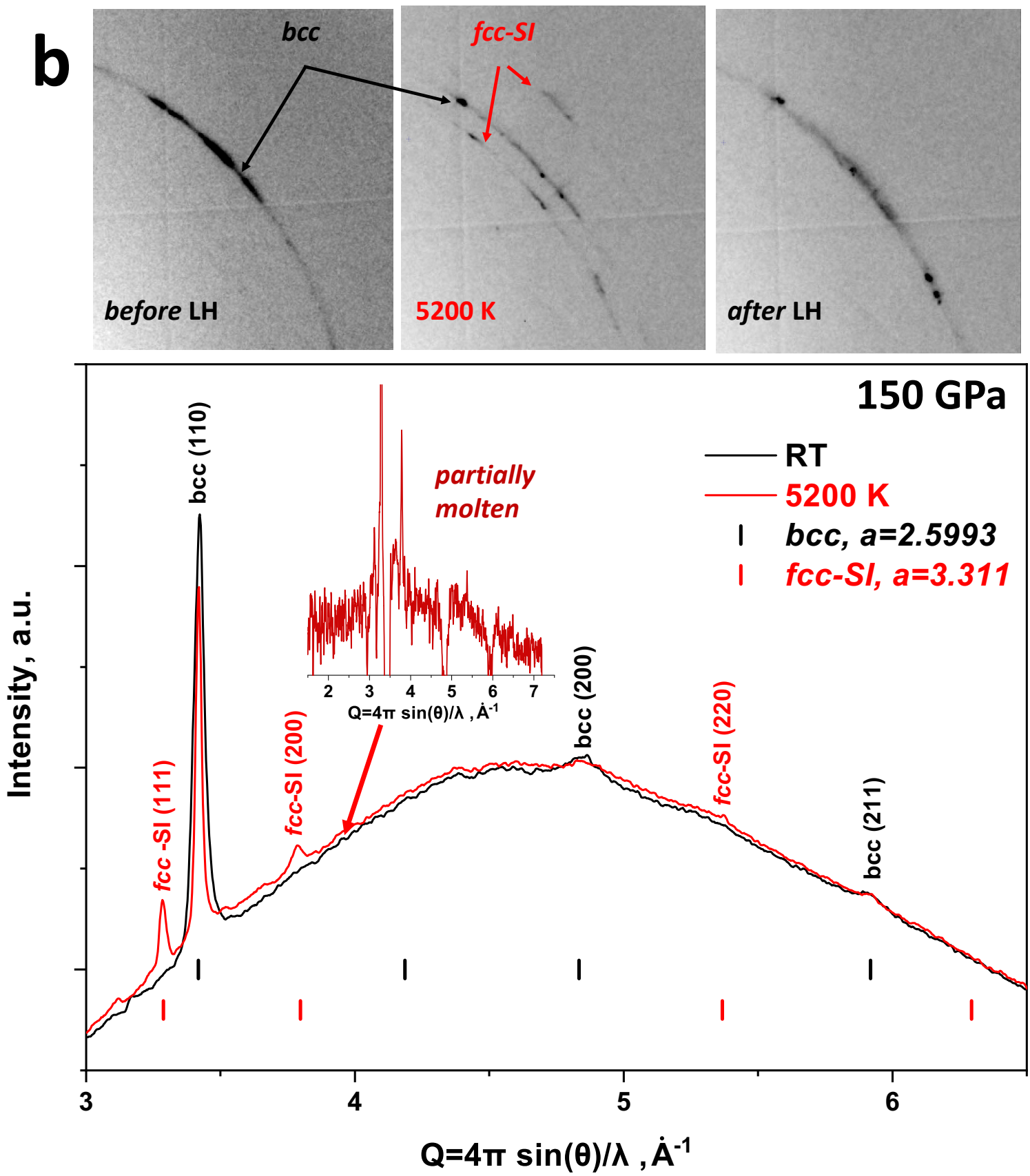
b
bcc
fcc-SI
before LH
5200 K
after LH
150 GPa
RT
5200 K
bcc, a=2.5993
fcc-SI, a=3.311
partially molten
Q=4π sin(θ)/λ ,Å-1
bcc (110)
fcc -SI (111)
fcc-SI (200)
bcc (200)
fcc-SI (220)
bcc (211)
Intensity, a.u.
Q=4π sin(θ)/λ ,Å-1

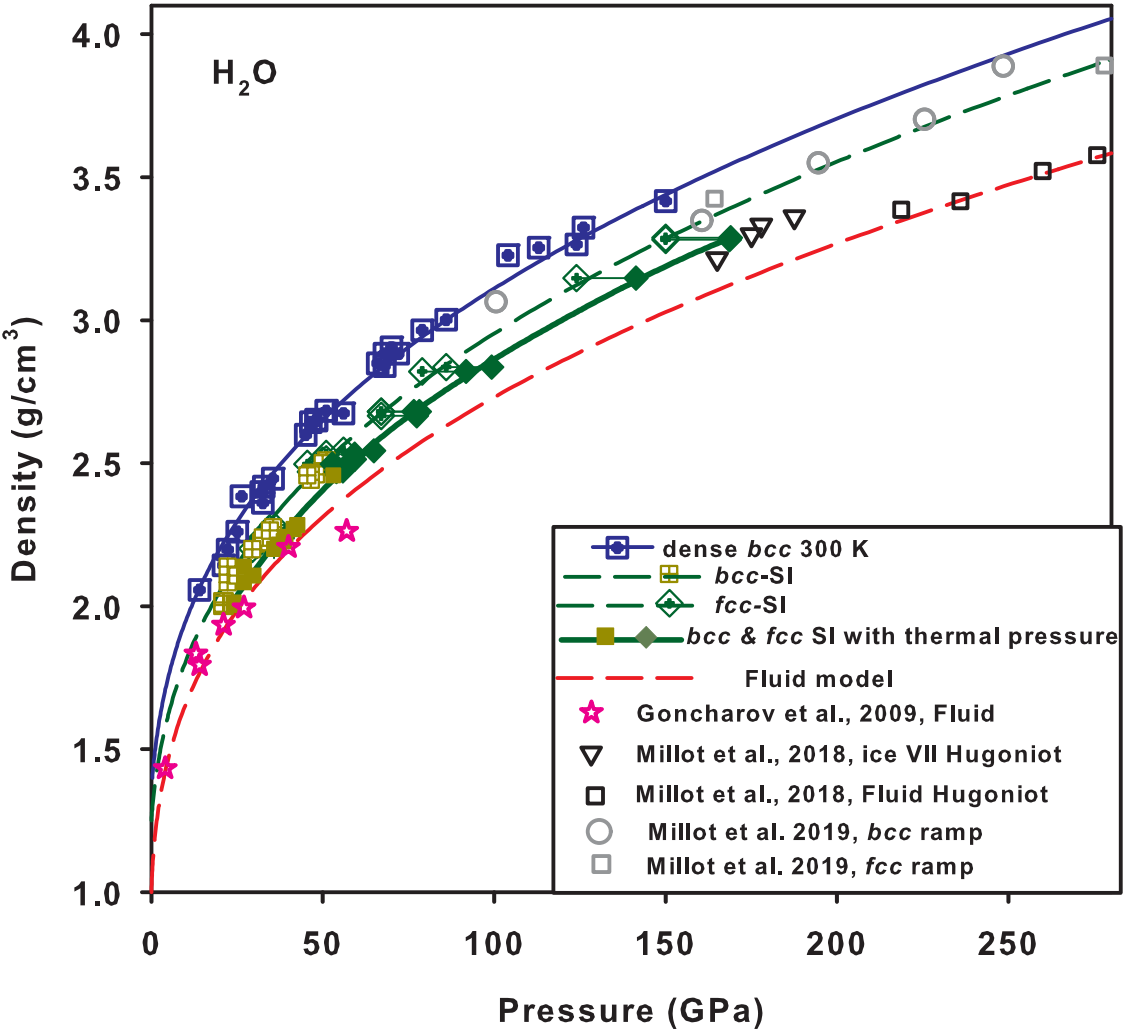
H2O
Density (g/cm3)
Pressure (GPa)
4.0
3.5
3.0
2.5
2.0
1.5
1.0
0
50
100
150
200
250
dense bcc 300 K
bcc-SI
fcc-SI
bcc & fcc SI with thermal pressure
Fluid model
Goncharov et al., 2009, Fluid
Millot et al., 2018, ice VII Hugoniot
Millot et al., 2018, Fluid Hugoniot
Millot et al. 2019, bcc ramp
Millot et al. 2019, fcc ramp

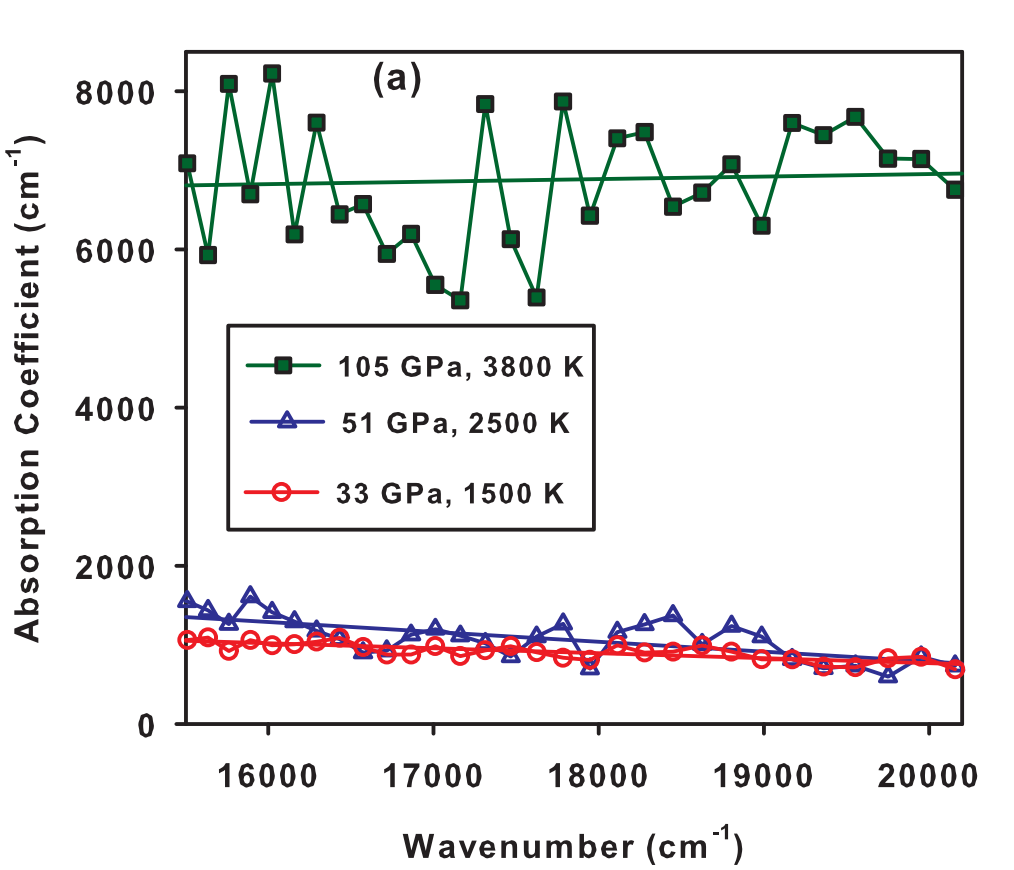
(a)
105 GPa, 3800 K
51 GPa, 2500 K
33 GPa, 1500 K
Absorption Coefficient (cm-1)
Wavenumber (cm-1)
0
2000
4000
6000
8000
16000
17000
18000
19000
20000

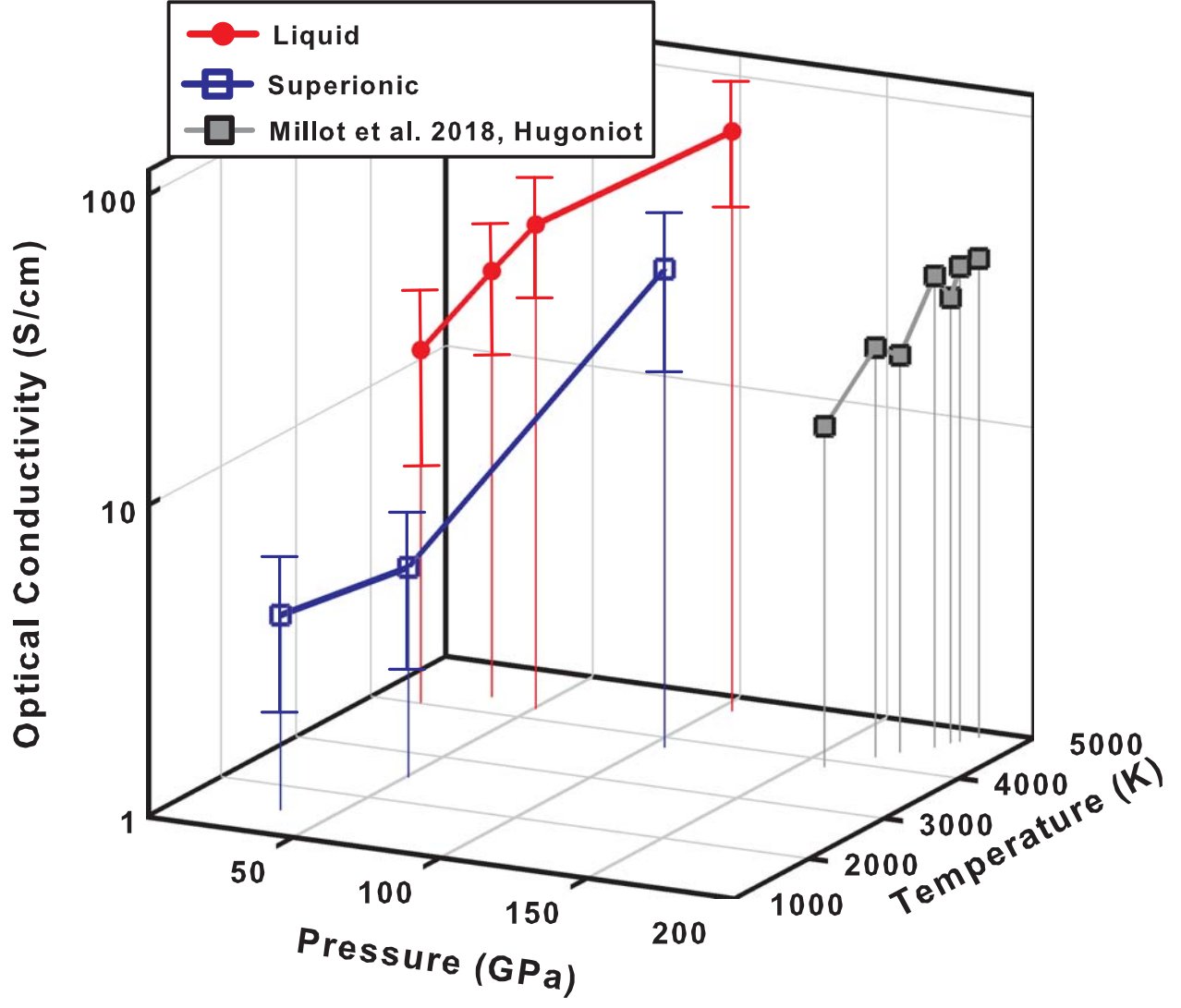
Liquid
Superionic
Millot et al. 2018, Hugoniot
Optical Conductivity (S/cm)
100
10
1
50
100
150
200
Pressure (GPa)
1000
2000
3000
4000
5000
Temperature (K)